PAPER

Check for updates

Study on the crystal structure and properties of a new crystal form of 3-nitro-1,2,4-triazole-5-one (NTO)

Manman Wang, Xing Zhang, Zifeng Wang, Dongze Li, Shusen Chen and Qinghai Shu [ID] *

3-Nitro-1,2,4-triazole-5-one (NTO) has received wide attention and has applications owing to its excellent detonation performance and low sensitivity. A new crystal form of NTO was prepared *via* the solvent evaporation method and named γ-NTO. Its crystal properties were studied through single-crystal X-ray diffraction, and the results indicated that the unit cell of γ-NTO belongs to the monoclinic space group *Pc*, with eight molecules in the single unit cell. The density of this crystal is calculated to be 1.907 g cm^{-3}, which is higher than that of β-NTO and similar to that of α-NTO. The crystal morphology was calculated to be a polygonal shape with a symmetrical growth pattern using the reactive force field. Based on the analysis of reactive molecular dynamics, the thermal decomposition mechanism of different crystal forms of NTO was elucidated, and the results showed that γ-NTO demonstrates higher gas production, providing a successful way to enhance detonation performance. The results of IR and differential thermal analysis (DTA) support the above conclusions.

Introduction

3-Nitro-1,2,4-triazole-5-one (NTO) is considered a high-energy and low-sensitivity energetic material in the field of explosives. As one of the energetic compounds, NTO is characterized by low sensitivity to impact, friction, heat, and shock waves, and its energy level is close to RDX. It is a new type of energetic material that has received extensive attention.[1–3] Two polymorphic crystal structures of the NTO molecule are known: α and β forms.[4,5] α-NTO is prepared by slowly cooling the hot solution of NTO in various solvents (such as water) and then freezing it. This crystal structure of NTO is elongated needle-shaped and is ruptured by a cut perpendicular to the crystal axis. Generally, this form is considered the most stable but tends towards twinning, which destroys its safety performance.[6] For β-NTO, the most commonly used preparation process is the recrystallization method in a mixture of methanol or ethanol/dichloromethane solution. Unfortunately, β-NTO can only maintain its properties for 6 months, and after that period, it will transform back into α-NTO.[7] At present, there is no effective way to maintain its long-term stability, and its instability obstructs the practical application. These factors hinder the storage performance and safety of NTO as an energetic material.

School of Materials Science & Engineering, Beijing Institute of Technology, Beijing 100081, China. E-mail: qhshu121@bit.edu.cn

The crystal structure of matter always has an important impact on its physical and chemical properties. Therefore, it is necessary to further study the polymorphism property of NTO to obtain a more stable and high-energy insensitive energetic material that can meet the requirements of diverse battlefield environments. Polymorphism is common in energetic materials; therefore, research on crystal engineering of explosives has become a hot topic in controlling the performance of explosives.[8–12] Balancing the detonation performance and low sensitivity of energetic materials is a crucial research topic to further enhance their application value.[13,14] Previous studies have shown that many factors, for example, the dipole moment of the solution, temperature, solvent/non-solvent ratio, and stirring methods, can affect the formation of crystal forms.[15–21] Various energetic materials, including 1,3,5-trinitro-1,3,5-triazinane (RDX), 1,3,5,7-tetranitro-1,3,5,7-tetrazocane (HMX), and 2,4,6,8,10,12-hexanitro-2,4,6,8,10,12-hexaazaisowurtzitane (CL-20) are found to be polymorphic.[8,22–28] Korsunskii *et al.*[29] first found ε-HMX in cyclohexanone with a strict experimental environment as a by-product in the preparation of phase transition. Liu *et al.*[30,31] carried out a comprehensive calculation of the molecular structure and mechanism of energetic materials. Furthermore, the thermal decomposition mechanism of HMX with polymorphism is explained by simulation. Zhang *et al.*[32] provided a systematic review of crystallization methods for energetic materials. Tan *et al.*[33] prepared a co-crystal of CL-20 and studied the related properties from the perspective of

molecular interaction. Chauhan *et al.*[34] converted the CL-20 of different crystal forms into the ε-form with better thermal stability and detonation performance by recrystallization. These studies have important implications for the development of energetic materials.

Due to the stretching, compression and rotation of the organic bonds, energetic materials possess different molecular conformations.[35–38] The diversity of conformations and weak intermolecular forces causes various crystal packing patterns, which lead to the formation of multiple crystal forms.[39–41] Then, different packing densities are presented and directly exhibit an important impact on the density, sensitivity, and thermal stability of energetic materials.[42] They affect the filtration, drying, and other processes in the production process of explosives, as well as the performance of energy, safety, mechanics, compatibility, and detonation in the application.[43] Based on this, the polymorphism can be used to change the crystal parameters of NTO, thereby effectively improving the performance drawbacks of NTO elements with targeted effects.

In the present study, we prepared a new crystal form of NTO (γ-NTO), and the crystal structure was analyzed by applying an X-ray single-crystal diffraction method. Crystal morphology and thermal decomposition mechanisms were calculated using molecular dynamics (MD) and reaction molecular dynamics (ReaxFF MD) methods. The qualitative analysis of different crystal forms was achieved by applying infrared spectroscopy, and the thermal stability and gas production were calculated and analyzed using thermal analysis. NTO provides a novel direction for research on NTO, and this work is expected to contribute to the process of thermal decomposition.

Experimental details

Materials

Raw NTO is prepared by Gansu Yin Guang Chemical Industry Group Co., Ltd., China. The average particle size of NTO ranges from 80 μm to 150 μm. 5-Amino-1,2,4-triazole-3-one (ATO) and anhydrous methanol are purchased from Shanghai Aladdin Bio-Chem Technology Co., Ltd., China.

Experimental methods

Solvent evaporation is a common method used to prepare single crystals.[28,32] Various crystals of energetic materials are completely obtained.[44–46] Single crystal grains of α-NTO and β-NTO are grown using this method.[5] At the ambient temperature (25 °C), NTO (5.0 mg) is dissolved in anhydrous methanol (5.0 mL). ATO is added as an additive to control the morphology, and the molar ratio of NTO and ATO is 1 : 1. The crystallization system is conducted by blending the solution under ultrasonic stirring until the mixture dissolves entirely. It is necessary to continue ultrasonication for 10 min to disperse the solute for a homogeneous solution. The treated solution is placed for a period of several days to evaporate the solvent at room temperature, and crystalline γ-NTO is formed.

Characterization methods

Crystal structure and lattice parameters are obtained with single crystal X-ray diffraction (SC-XRD) by applying Bruker D8 Venture at 293 K (Cu Kα radiation, graphite monochromator). The crystal data of α-NTO and β-NTO are available from the Cambridge structural database. Materials Studio (MS, 2018) is used to calculate the properties of NTO crystal faces and morphology with the COMPASS II force field. The thermal decomposition mechanism of different crystal forms of NTO is simulated by MAPS with the new ReaxFF-lg force field developed by Du *et al.*[47] The Fourier transform infrared (FTIR) spectrum is collected by applying Bruker ALPHA II. The rate of scanning is 4 cm^{-1} in a range of 400–4000 cm^{-1}. Differential thermal analysis (DTA) is widely used in the analysis and testing of crystal thermal decomposition and thermodynamic behavior with high testing efficiency and sensitivity. The analysis of thermal stability and weight loss *vs.* temperature is performed by thermogravimetric analysis–differential thermal analysis (TG–DTA, Shimadzu DTG-60). 0.7–1.0 mg of samples are heated in an alumina crucible at a heating rate of 10 °C min^{-1} from 50 to 450 °C.

Results and discussion

Crystal structure

The lattice parameters of γ-NTO are recorded by SC-XRD. The accurate crystal structure of γ-NTO was confirmed with SC-XRD. The crystallographic data are presented in Table 1. The crystal belongs to the monoclinic system with space group *Pc*. 8 molecules are contained in a unit cell, and this result is evidently different from those of α-NTO and β-NTO, representing a new crystal belonging to NTO prepared in this study. It is known that the values of density for α-NTO and β-NTO are 1.903 g cm^{-3} and 1.876 g cm^{-3}, respectively.[48] After verification, the density of γ-NTO (1.907 g cm^{-3}) is higher than that of β-NTO and similar to that of α-NTO, and this is considered to be a crystal structure for NTO with high energy levels.[49]

The molecular stacking structure and intermolecular distance of γ-NTO are shown in Fig. 1. In the crystal structure, intermolecular hydrogen bonds are observed between the

Table 1 Lattice parameters of γ-NTO

Crystal polymorph	γ-NTO
Temperature (K)	293(2)
Crystal system	Monoclinic
Space group	*Pc*
Z	8
a (Å)	5.13(4)
b (Å)	10.33(9)
c (Å)	17.30(16)
β (°)	98.42(3)
Volume (Å^3)	905.97(14)
Density (g·cm^{-3})	1.907

Fig. 1 Molecular stacking structure and intermolecular distance of γ-NTO.
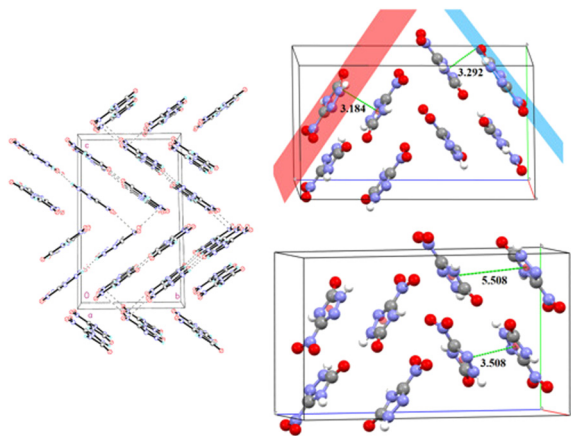
Fig. 2 Bond interaction of NTO: (a) populations of close interatomic contacts; (b) Hirshfeld surface; and (c–e) two-dimensional fingerprint plots of NTO.
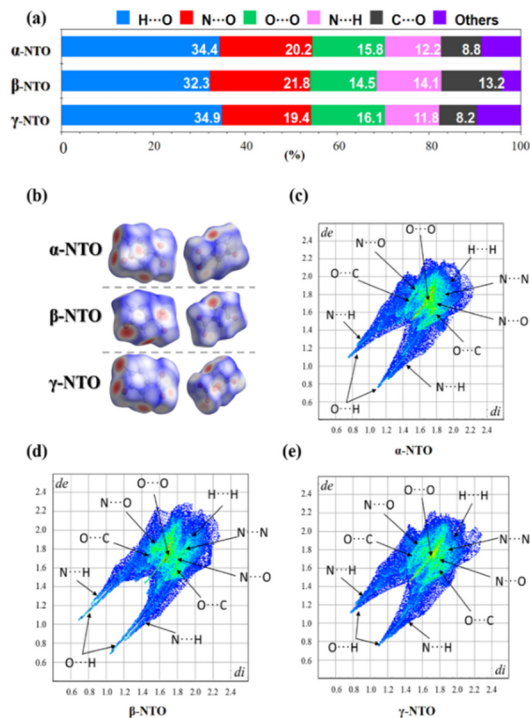
oxygen atoms on the nitro and carbonyl groups and the hydrogen atoms on the azole ring. Meanwhile, there is an interaction between the N and O of the nitro group in different molecules. Fig. 1 illustrates that γ-NTO exhibits W-type planar-layered structure and the structure packs tightly. In addition, layers are connected by N⋯O interaction without hydrogen bonding, whereas strong hydrogen bonding interaction exists only in the same layer. The vertical distances between the molecular layers are 3.292 Å and 3.184 Å. The distances of the centroids are 3.508 Å and 5.508 Å, respectively. A distance less than 3.8 Å is considered to possess a face-to-face π–π stacking effect, which has benefits for low impact sensitivity or fine thermal stability.

The close interactions of the interatomic contacts are counted, as depicted in Fig. 2. The Hirshfeld surface clearly illustrates the intermolecular interaction. The intermolecular in atomic contacts is characterized by colour distribution with a large number of points. Red and blue represent the high and low intensities of interaction, respectively.[30,35,50] In the two-dimensional fingerprint plots, the decreasing order of close contact is H⋯O > N⋯O > O⋯O > N⋯H > C⋯O. Combined with the Hirshfeld surface, strong interactions appear between NO_2 or carbonyl and hydrogen on the triazole ring. The interaction on the carbonyl group is stronger than that of NO_2, constituting a stable structure. Meanwhile, the difference in interatomic contact affects the stability of the crystal structure. The population of C⋯O in β-NTO is 5% higher than that in the other forms, which replaces the interaction of H⋯O. The Hirshfeld surface explains the acidity of β-NTO with the obvious change in the red area on the 1-position H, performing weak interaction for an unstable structure. In contrast, α- and γ-NTO tend to be stable.

Morphology

The COMPASS II force field is combined with quantum mechanical computation for comprehensive data as an expanded force field of COMPASS. In the COMPASS force field, various energetic materials are fitted with the force field, except for NTO. The new parameters of COMPASS II can solve the problem that the inappropriate N force field type is assigned for N–H at the triazole ring in the original COMPASS, which is verified to break the planar structure of NTO. The geometry optimization of NTO unit cells with different crystal forms is performed by Forcite. The summation method of electrostatic is Ewald with 10^{-4} kcal mol^{-1} accuracy, and the cutoff distance is 15.5 Å for the calculation of van der Waals interaction using the atom-based truncation method. The maximum relative error between the actual data and the simulated data is less than 15%. The optimized unit cell is analyzed using the growth morphology method in the morphology module. The morphology of the crystal and the parameters of the main crystal faces of γ-NTO are displayed in Fig. 3 and Table 2,
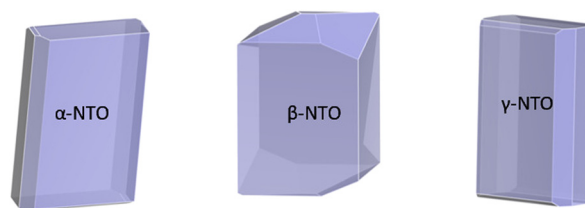

Fig. 3 Prediction of the crystal morphology of NTO with different crystal forms in vacuum.

Table 2 Parameters of main crystal faces of γ-NTO

Facet	Multiplicity	$E_{att}/(kJ\ mol^{-1})$	$S/\%$
(0 0−2)	1	−40.85	21.57
(0 0 2)	1	−40.85	21.57
(0 1 0)	2	−66.80	13.51
(0 1 1)	2	−67.34	11.11
(0 1−1)	2	−67.34	11.11
(−1 0 0)	1	−104.73	8.17
(1 0 0)	1	−104.73	8.17
(1 0−2)	1	−105.77	1.20
(−1 0 2)	1	−105.77	1.20
(−1 0−2)	1	−105.77	1.20
(1 0 2)	1	−105.77	1.20

respectively. The attachment energy (E_{att}) determines the degree of crystallization in a vacuum. 11 main crystal faces of γ-NTO are listed in Table 2, which is simulated in a vacuum. The sum of the area percentages of 7 main faces exceeds 95%, among which the (0 0 2) and (0 0−2) faces account for the largest facet area of 21.57%. Based on previous studies, α-NTO and β-NTO possess 4–6 main faces in different force fields. Concurrently, the largest facet area is above 50%, which eventually makes the growth of crystals present a tendency toward fragile needle-like or plate-like shape. It can be observed from Fig. 3 that γ-NTO has a polygonal shape with a symmetrical growth mode. The proportion of each crystal face is relatively average, which favours the growth of crystals with higher sphericity.

Simulation of the thermal decomposition mechanism

The ReaxFF-lg force field of MAPS software is based on a large-scale atomic/molecular massively parallel simulator (LAMMPS), which can accurately predict the most energetic material crystals. However, the potential functions of the force field are not suitable for thermal decomposition simulation for NTO, which affects the accuracy of the results. Du et al.[47] built a set of new ReaxFF-lg parameters to solve the problem. The three crystal forms were established as 4 ×

Fig. 4 Simulation results: (a) diagrammatic sketch; (b) the variation curve of NTO content of different crystal forms.

3 × 2, 3 × 4 × 4, and 4 × 3 × 2 supercell models, as shown in Fig. 4(a). The red, blue, gray, and white balls in Fig. 4 represent the O, N, C, and H elements, respectively. The atomic positions are optimized to obtain the minimum energy structure using the steepest descent method. The reactive molecular method is used to simulate the optimized structure with the NVT ensemble. A primary simulation of 5 ps is performed to relax the system; then, the reaction temperature is set from 298 K to 2298 K with a Berendsen thermostat. The simulation duration is 50 ps, and the time step is 0.1 fs.

Fig. 4(b) shows the process of decomposition of NTO. It can be observed that compared with α-NTO and β-NTO, the decomposition of γ-NTO presents a distinct staged reaction. Nearly 40% of γ-NTO react first and decompose partly in the initial few seconds. During the next 10 ps, the content of γ-NTO fluctuated continuously at a value of 5%. The reaction path of NTO was considered to have three main steps: proton transfer, denitrification, and formation of clusters. The significant change in content indicates that reversible reactions occur in γ-NTO. Proton transfer and the gathering of clusters are considered possible steps in the reaction path.

Afterward, the trend of γ-NTO content is not significantly different from the other crystal forms. α-NTO begins to decompose at about 10 ps, and the primary reaction of β-NTO appears at about 15 ps. All the reactions finish within 40 ps, which indicates that β-NTO possesses a faster response speed than α-NTO and γ-NTO after the beginning of decomposition.

The reactive molecular dynamics method can simulate the physical and chemical processes of systems containing millions of atoms under different external loading conditions in a short computational time, providing detailed and accurate information at the atomic and molecular scales. The simulation process is as follows. First, the model is geometrically optimized to obtain a reasonable initial configuration. Then, the optimized system is heated to ensure that the crystals do not decompose during the heating process. After reaching the target temperature at $T = 2298$ K, isothermal isovolumetric molecular dynamics simulation (NVT-MD) was performed. The Berendsen method is used to adjust the temperature to fluctuate around the set value. All calculations in this article use periodic boundary conditions, with a simulation time step of 0.1 fs and a simulation time of 50 ps. Within 50 ps, all the main decomposition products appeared and were sufficient to describe the primary and secondary chemical reactions, as well as the influence of pressure on the reaction mechanism. Fig. 5 shows the evolution of NTO decomposition. The main gas product is shown in Fig. 5(a). In the first 20 ps, there are almost no gaseous products, indicating that it is difficult for NTO to undergo denitrification in the initial stage of decomposition. This is because a large energy barrier in the reaction and high temperature is required to satisfy the conditions. The intermediate products obtained by proton transfer also participate in denitrification, indicating that the reaction
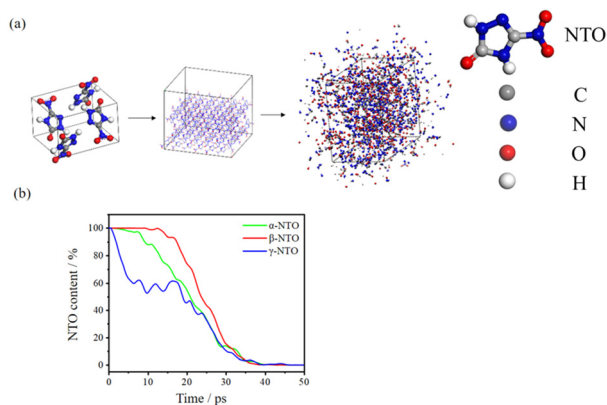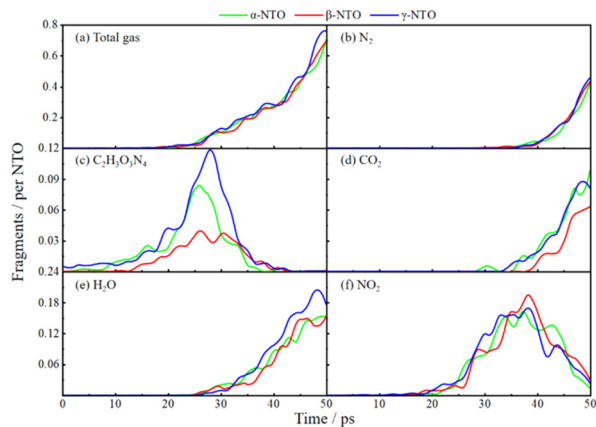
Fig. 5 Thermal decomposition situation: (a) total gas: (b) $C_2H_3O_3N_4$; (c) CO_2; (d) H_2O; (e) N_2; and (f) NO_2.

Table 3 Part reactions of NTO in different crystal forms

	Reaction numbers		
Reactions	α-NTO	β-NTO	γ-NTO
$C_2H_2O_3N_4 \rightarrow C_2H_2ON_3 + NO_2$	24	28	22
$2C_2H_2O_3N_4 \rightarrow C_2H_3O_3N_4 + C_2HO_3N_4$	21	4	26
$C_2H_3O_3N_4 \rightarrow C_2H_3ON_3 + NO_2$	8	4	9
$nC_2H_2O_3N_4 \rightarrow (C_2H_2O_3N_4)_n$	58	69	14
$C_2H_2ON_2 \rightarrow C_2HON_2 + NH$	7	2	—
$C_2H_2O_3N_4 \rightarrow C_2HO_3N_3 + NH$	1	5	—
$C_2H_2O_3N_4 + H \rightarrow CH_3ON_2 + CO_2N_2$	1	—	11

may occur within 25 ps with a decrease in $C_2H_3O_3N_4$. This time is also shown by the upward trend of NO_2 in Fig. 5(f). The final gas content of γ-NTO is about 10% higher than those of the other crystal forms, illustrating that the unique reaction path of γ-NTO can produce more gas, which is beneficial to the improvement of detonation velocity and pressure. Fig. 5(b)–(f) illustrates the time-dependent curves of some products of the thermal decomposition of NTO. The amount of intermediate product $C_2H_3O_3N_4$ is almost three times of β-NTO and significantly higher than that produced by α-NTO, as depicted in Fig. 5(c). γ-NTO is partially converted into $C_2H_3O_3N4$ in an early reaction. Moreover, the number of fragmented products is evidently less than that of NTO, as shown in Fig. 4(b), which suggests that proton transfer and formation of clusters occur during the γ-NTO reaction. In Fig. 5(d), it can be observed that the CO_2 content of β-NTO is lower, while the generation time is longer than those of the other crystal forms, illustrating that β-NTO has different reaction paths in producing CO_2. As shown in Fig. 5(e), the final content of H_2O in γ-NTO is slightly higher than in the others, and the number of H_2O molecular fragments presents a clear upward trend at 45 ps without a visible difference in the prophase, which confirms the different reaction paths to generate H_2O at the telophase of the reaction in γ-NTO. It is found in Fig. 5(b) that the variation trend of N_2 slightly differs from each other during the decomposition, while Fig. 5(f) concurrently describes that the maximum amount of NO_2 produced by β-NTO is larger than the others. Under high temperatures, the mutual conversion between nitrogen oxides frequently occurs and causes the amount of NO_2 fragments to fluctuate greatly, eventually becoming steady N_2 or integrating with H fragments to H_2O. Most NO_2 exists only as an intermediate product of the reaction.

The statistical analysis of bond formation and breakage in the reaction process and some of the main reactions obtained are shown in Table 3. According to the reaction numbers, γ-NTO tends to undergo a proton transfer reaction rather than form clusters, while a large portion of α- and

β-NTO form clusters. Compared with the other crystal forms, β-NTO is less prone to proton transfer. The number of reactions in the denitrification of each form is basically the same, indicating that the crystal form has no obvious effect on denitrification.

In addition, the different crystal forms lead to different reaction paths. Combining the product contents, the thermal decomposition reaction paths of the three crystalline NTO are shown in Fig. 6. First, the proton transfer reaction of H appears between two NTO molecules to form intermediate products $C_2HO_3N_4$ and $C_2H_3O_3N_4$ in path A. Between the C on C–NO_2 groups and adjacent N, the ring-opening reaction produces unstable fragments and finally decomposes into HON, CO, N_2, and other gas products by bond breaking. In addition, the strong electron-withdrawing effect of the nitro and carbonyl groups in the NTO molecule decreases the electron cloud density of the adjacent 4-position nitrogen atom, which leads to ionizing the H on the nitrogen atom. Both the dehydrogenated and initial NTO can form NTO clusters as the second reaction path. Meanwhile, the third common reaction path is denitrification for separating NO_2 from NTO and forms $C_2H_2ON_3$, which opens the ring into the three-membered ring system of N–C–N and eventually breaks bonds to produce CO, N_2, NH_3, H_2O, etc. In α-NTO, the ring-opening reaction of NTO tends to arise on 3-position C or 5-position C with four-position N after denitrification, while the reaction is more likely to occur without denitrification in β-NTO, but both α-NTO and β-NTO generate NH to participate in intermediate reactions. However, the above reaction paths do not appear in γ-NTO instead of opening the ring at other positions to produce $NHCONH_2$
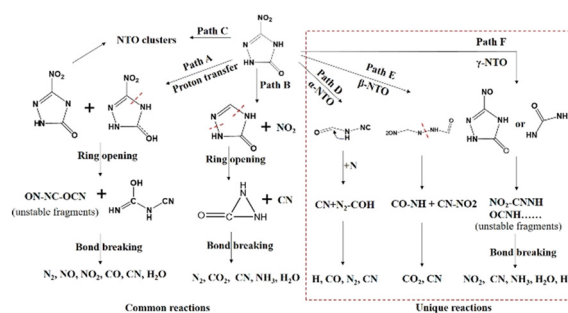

Fig. 6 Thermal decomposition paths of NTO.

combined with H. Simultaneously, the O on the nitro group escapes, and the free radical exists for a very short time, which opens the ring to generate gaseous fragment products, such as NH_3, CN, and NO_2. In addition, it can be observed from Fig. 5(c) that γ-NTO generates a large amount of $C_2H_3O_3N_4$ in the initial reaction as an intermediate product of proton transfer, which affects the reaction path of γ-NTO.

FTIR spectroscopy

The IR spectrum can determine the characteristic peaks of each group in the materials, which has a dominant advantage in the qualitative and semi-quantitative characterization of material category information. The IR spectra of α-NTO, β-NTO and γ-NTO are presented in Fig. 7. The peaks around 3000–3260 cm^{-1} are identified as N–H stretching vibration peaks, while the peaks at 1700 cm^{-1} are C=O stretching vibration peaks. As shown in Fig. 7(a), there is no obvious difference in the characteristic peaks between the three crystal forms, which infer the same chemical group and substance. However, there is a difference in the C=O stretching vibration peaks in Fig. 7(b). Compared with α-NTO and β-NTO, γ-NTO exhibits a clear bimodal pattern, which proves that there are two chemical environments for the carbonyl group. Combined with Fig. 5, the reason for the decomposition of γ-NTO at the initial stage is speculated to be that different environments discriminate the electron withdrawing ability for a trend of proton transfer. This conclusion is also supported by the increase in the initial intermediate content, as shown in Fig. 5(c).

Thermal analysis

TG curves and the corresponding DTG results of α-NTO, β-NTO, and γ-NTO samples are shown in Fig. 8(a) and (b), respectively. As shown in Fig. 8, for α-NTO, the exothermic reaction began at 242.5 °C, with a weight loss rate of 75.82%. Two exothermic peaks corresponding to faster decomposition rates appeared at 267.1 °C and 275.4 °C. For β-NTO, the exothermic reaction began at 246.9 °C, with a thermal weight loss rate of 74.91%. The peak with the fastest decomposition rate corresponds to a temperature of 272.6 °C. The initial reaction temperature of γ-NTO is 250.0 °C, and the total weight loss rate is 78.65%. The reaction exhibits two peaks
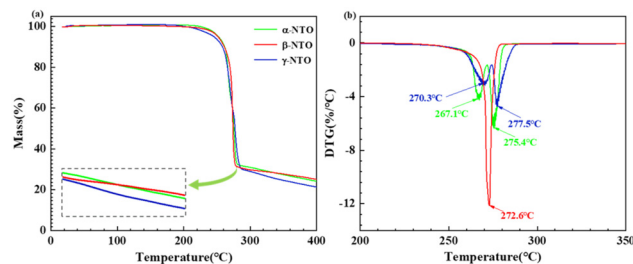

Fig. 8 TG curves of α-NTO, β-NTO, and γ-NTO (a) and (b) DTG curves.

with faster decomposition rates, corresponding to 270.3 °C and 277.5 °C.

Compared with α-NTO and β-NTO, γ-NTO is approved for a relatively higher thermal decomposition temperature and higher thermal decomposition weight percent. These results indicated that the corresponding thermal decomposition process of the as-prepared γ-NTO was performed more thoroughly, which can release higher energy. This should be due to the high amount of intermediate product $C_2H_3O_3N_4$ in the thermal decomposition process for the γ-NTO molecules.

Conclusions

In this study, a new crystal form of NTO, γ-NTO, is obtained in anhydrous methanol by solvent evaporation. γ-NTO tends to grow in the direction of higher sphericity than the other crystal forms, and the crystal facet growth is symmetric in a vacuum. Common reactions and unique reactions are obtained by ReaxFF-MD simulations. The thermal decomposition reaction paths are influenced by the different crystal forms of NTO. α-NTO and β-NTO tend to form clusters, while the path is replaced by proton transfer in γ-NTO. Meanwhile, the path of γ-NTO generates more gas products for better explosive performance. In addition, the decomposition mechanism of γ-NTO is tested and confirmed using infrared and thermogravimetric methods. Overall, compared with the other crystal forms, γ-NTO has the same thermal stability and higher gas production for the contribution of detonation velocity and pressure.

Author contributions

Manman Wang: methodology, investigation, conceptualization, visualization, data curation, formal analysis, software, writing original draft, writing – review & editing. Xing Zhang: data curation, formal analysis, writing – review & editing. Zifeng Wang: methodology, formal analysis, software, writing – review and editing. Dongze Li: data curation, formal analysis, software, methodology. Shusen Chen: methodology, conceptualization, supervision, visualization. Qinghai Shu: resources, supervision, conceptualization, supervision, visualization, writing – review & editing.
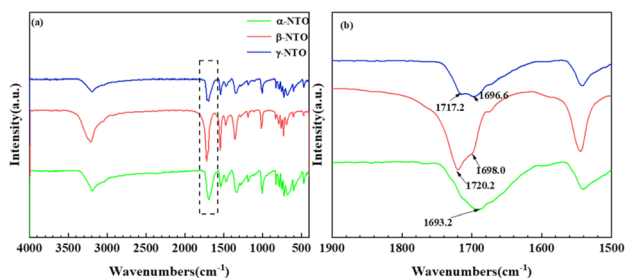
Fig. 7 IR spectra of (a) α-NTO, β-NTO and γ-NTO and (b) characteristic peak.

Conflicts of interest

There are no conflicts to declare.

Acknowledgements

References

1 G. Lan, J. Li, G. Zhang, J. Ruan, Z. Lu, S. Jin, D. Cao and J. Wang, *Fuel*, 2021, **295**, 120655.

2 S. Hanafi, D. Trache, S. Abdous, Z. Bensalem and A. Mezroua, *J. Energ. Mater.*, 2019, **27**(04), 326–347.

3 G. Lan, X. Li, H. Chao, N. Wang, C. Wei, Z. Li and J. Wang, *J. Chem. Eng. Data*, 2021, **66**(10), 3897–3910.

4 N. Bolotina, K. Kirschbaum and A. A. Pinkerton, *Acta Crystallogr., Sect. B: Struct. Sci.*, 2005, **61**(5), 577–584.

5 E. A. Zhurova and A. A. Pinkerton, *Acta Crystallogr., Sect. B: Struct. Sci.*, 2001, **57**, 359–365.

6 K. Zhong, R. Bu, F. Jiao, G. Liu and C. Zhang, *Chem. Eng. J.*, 2022, **429**, 132310.

7 E. N. Rao and V. K. Rao, *J. Phys.: Condens. Matter*, 2023, **35**, 065401.

8 J. J. Brady, B. L. Argirakis, A. D. Gordon, R. T. Lareau and B. T. Smith, *Appl. Spectrosc.*, 2018, **72**(1), 28–36.

9 R. M. Eason and T. D. Sewell, *J. Dyn. Behav. Mater.*, 2015, **1**(4), 423–438.

10 S. Hunter, P. L. Coster, A. J. Davidson, D. I. A. Millar, S. F. Parker, W. G. Marshall, R. I. Smith, C. A. Morrison and C. R. Pulham, *J. Phys. Chem. C*, 2015, **119**(5), 2322–2334.

11 J. L. Mendoza-Cortes, Q. An, W. A. Goddard, C. Ye and S. Zybin, *J. Comput. Chem.*, 2016, **37**(2), 163–167.

12 B. Pan, H. Wei, J. Jiang, S. Zong, P. Lv and L. Dang, *J. Mol. Liq.*, 2018, **265**, 216–225.

13 Y. Cao, W. Lai, T. Yu, Y. Liu and B. Wang, *FirePhysChem*, 2021, **1**(1), 27–32.

14 J. T. Wu, J. G. Zhang, T. Li, Z. M. Li and T. L. Zhang, *RSC Adv.*, 2015, **5**(36), 28354–28359.

15 G. J. O. Beran, J. D. Hartman and Y. N. Heit, *Acc. Chem. Res.*, 2016, **49**(11), 2501–2508.

16 Z. Gao, S. Rohani, J. Gong and J. Wang, *Engineering*, 2017, **3**(3), 343–353.

17 R. V. Kent, R. A. Wiscons, P. Sharon, D. Grinstein, A. A. Frimer and A. J. Matzger, *Cryst. Growth Des.*, 2017, **18**(1), 219–224.

18 K. B. Landenberger, O. Bolton and A. J. Matzger, *J. Am. Chem. Soc.*, 2015, **137**(15), 5074–5079.

19 Z. Wu, S. Yang and W. Wu, *CrystEngComm*, 2016, **18**(13), 2222–2238.

20 L. Xiao, S. Guo, H. Su, B. Gou, Q. Liu, G. Hao, Y. Hu, X. Wang and W. Jiang, *RSC Adv.*, 2019, **9**(16), 9204–9210.

21 H. Xu, X. Duan, H. Li and C. Pei, *RSC Adv.*, 2015, **5**(116), 95764–95770.

22 A. M. Figueroa-Navedo, J. L. Ruiz-Caballero, L. C. Pacheco-Londoño and S. P. Hernández-Rivera, *Cryst. Growth Des.*, 2016, **16**(7), 3631–3638.

23 J. J. Brady, B. L. Argirakis, A. D. Gordon, R. T. Lareau and B. T. Smith, *Appl. Spectrosc.*, 2016, **72**(1), 28–36.

24 M. Ghosh, S. Banerjee, M. A. S. Khan, N. Sikder and A. K. Sikder, *Phys. Chem. Chem. Phys.*, 2016, **18**(34), 23554–23571.

25 X. He, Y. Liu, S. Huang, Y. Liu, X. Pu and T. Xu, *RSC Adv.*, 2018, **8**(41), 23348–23352.

26 R. Kumar, P. F. Siril and P. Soni, *J. Energ. Mater.*, 2015, **33**(4), 277–287.

27 W. Liang, J. Wang, H. Liu, Z. Meng, L. Qiu and S. Wang, *Powder Technol.*, 2022, **395**, 732–742.

28 P. Zou, X. Wang, L. Zhang, R. Dai, Z. Wang, Y. Liu, Z. Zhang, S. Huang and J. Tan, *J. Phys. Chem. C*, 2021, **125**(22), 12390–12397.

29 B. L. Korsunskii, S. M. Aldoshin, S. A. Vozchikova, N. I. Golovina, N. V. Chukanov and G. V. Shilov, *Russ. J. Phys. Chem. B*, 2011, **4**(6), 934–941.

30 G. Liu, R. Gou, H. Li and C. Zhang, *Cryst. Growth Des.*, 2018, **18**(7), 4174–4186.

31 G. Liu, B. Tian, S. Wei and C. Zhang, *J. Phys. Chem. C*, 2021, **125**(18), 10057–10067.

32 X. X. Zhang, Z. J. Yang, F. Nie and Q. L. Yan, *Energ. Mater. Front.*, 2020, **1**(3–4), 141–156.

33 Y. Tan, Z. Yang, H. Wang, H. Li, F. Nie, Y. Liu and Y. Yu, *Cryst. Growth Des.*, 2019, **19**(8), 4476–4482.

34 B. S. Chauhan, A. Thakur, P. K. Soni and M. Kumar, *IOP Conf. Ser.: Mater. Sci. Eng.*, 2021, **1033**(1), 012056.

35 R. Bu, H. Li and C. Zhang, *Cryst. Growth Des.*, 2020, **20**(5), 3561–3576.

36 J. C. Bennion and A. J. Matzger, *Acc. Chem. Res.*, 2021, **54**(7), 1699–1710.

37 R. Rajan, T. R. Ravindran, V. Venkatesan, V. Srihari, K. K. Pandey, S. Chandra, K. K. Mishra and A. A. Vargeese, *J. Phys. Chem. A*, 2018, **122**(30), 6236–6242.

38 C. C. Ye, Q. An, W. Q. Zhang and W. A. Goddard, *J. Phys. Chem. C*, 2019, **123**(14), 9231–9236.

39 J. Zhang, L. A. Mitchell, D. A. Parrish and J. M. Shreeve, *J. Am. Chem. Soc.*, 2015, **137**(33), 10532–10535.

40 J. Zhang and J. M. Shreeve, *CrystEngComm*, 2016, **18**(33), 6124–6133.

41 G. Li and C. Zhang, *J. Hazard. Mater.*, 2020, **398**, 122910.

42 A. A. Gidaspov, V. V. Bakharev, K. Y. Suponitsky, V. G. Nikitin and A. B. Sheremetev, *RSC Adv.*, 2016, **6**(106), 104325–104329.

43 B. M. Abraham, J. P. Kumar and G. Vaitheeswaran, *ACS Omega*, 2018, **3**(8), 9388–9399.

44 M. Ghosh, A. K. Sikder, S. Banerjee and R. G. Gonnade, *Cryst. Growth Des.*, 2018, **18**(7), 3781–3793.

45 D. Herrmannsdörfer and T. M. Klapötke, *Cryst. Growth Des.*, 2021, **21**(3), 1708–1717.

46 J. V. Viswanath, B. Shanigaram, P. Vijayadarshan, T. V. Chowadary, A. Gupta, K. Bhanuprakash, S. R. Niranjana and A. Venkataraman, *Propellants, Explos., Pyrotech.*, 2019, **44**(12), 1570–1582.

47 L. Du, S. Jin, P. Nie, C. She and J. Wang, *Molecules*, 2021, **26**(16), 4808.

48 S. Hanafi, D. Trache, S. Abdous, Z. Bensalem and A. Mezroua, *Hanneng Cailiao*, 2019, **27**(4), 326–347.

49 J. Zhang, Z. Jin, W. Hao, Z. Guo, Y. Wang, R. Peng and B. Jin, *Cryst. Growth Des.*, 2023, **23**, 4499–4505.

50 M. Keikha, M. Pourayoubi and A. van der Lee, *J. Chem. Crystallogr.*, 2019, **50**(2), 88–98.